energies

MDPI

Article

Electrochemical Deposition of Multicomponent Mixed Metal Oxides on rGO/Ni Foam for All-Solid-State Asymmetric Supercapacitor Device: Mn, Co, and Ni Oxides with Ag Doping

Yunus Emre Firat [1,2] and Viktor Čolić [1,3,*]

[1] Electrochemistry for Energy Conversion, Max-Planck-Institute for Chemical Energy Conversion, Stiftstraße 34-36, D-45470 Mülheim an der Ruhr, Germany
[2] Physics Department, Kamil Ozdag Faculty of Sciences, Karamanoglu Mehmetbey University, Yunus Emre Campus, Karaman 70100, Turkey
[3] CENIDE—Center for Nanointegration Duisburg-Essen, University of Duisburg-Essen, D-47057 Duisburg, Germany
* Correspondence: viktor.colic@cec.mpg.de; Tel.: +49-208-379-82-35

Abstract: In this study, an asymmetric supercapacitor (ASSC) device is assembled by the deposition and annealing of silver-doped mixed metal oxides on reduced graphene oxide (rGO)/Ni foam and activated carbon (AC) on Ni foam as positive and negative electrodes, respectively. The best performing Ag:MnCoNiO active material is synthesized on rGO/Ni foam using chronopotentiometry combined with heat treatment. The XRD study clearly confirms the crystalline nature of the electrode with $MnCo_2O_4$ and $MnNi_2O_4$ phases. FT-IR and XPS studies revealed the formation of Ag:MnCoNiO/rGO on Ni foam. SEM images show a thin-film layer of fabricated material on the surface of rGO/Ni foam. The supercapacitor properties were tested in two- and three-electrode configurations, with cyclic voltammetry (CV), galvanostatic charge/discharge (GCD), and electrochemical impedance spectroscopy (EIS) experiments in a 6 M KOH aqueous electrolyte. In the three-electrode configuration, reversible faradic reactions can be observed in a potential range of 0.0 and +0.6 V vs. $Hg/HgSO_4$. In the two-electrode device configuration, the system exhibits a maximum energy density of 45.5 Wh kg^{-1} and provides a maximum power density of 4.5 kW kg^{-1}. The results showed that the doping of Ag in a MnCoNiO electrode shows promising properties, achieved by a very simple fabrication process. The results showcase the synergistic effects achieved by mixed multiple-component metal oxides, leading to improved supercapacitive properties.

Keywords: mixed metal oxide; supercapacitor; electrodeposition; specific capacitance; electrochemical impedance spectroscopy; cyclic voltammetry

Citation: Firat, Y.E.; Čolić, V. Electrochemical Deposition of Multicomponent Mixed Metal Oxides on rGO/Ni Foam for All-Solid-State Asymmetric Supercapacitor Device: Mn, Co, and Ni Oxides with Ag Doping. *Energies* **2022**, *15*, 8559. https://doi.org/10.3390/en15228559

Academic Editors: Desmond Gibson, Mojtaba Mirzaeian, Peter Hall and Saule Aidarova

Received: 25 October 2022
Accepted: 12 November 2022
Published: 16 November 2022

1. Introduction

The growth in the industry of portable electronic devices and electric vehicles has motivated extensive research aiming to develop practical energy storage systems [1–4]. In this regard, fuel cells and lithium-ion batteries are considered to be prominent candidates for energy storage in the foreseeable future. Supercapacitors (SCs) have emerged as an alternative for such devices [5–8] due to certain advantages, such as their low-cost fabrication, power density, rapid charge/discharge rate, and durability. Even so, their limited energy density is a major barrier for their further commercialization [9,10]. In this regard, the fabrication of innovative materials with suitable electrochemical properties to increase the energy density in these devices is a key challenge to be overcome [11,12].

The selection of electrode material plays a key role in SC performance, as it determines the capacitance of the device, which is grouped into two main categories (i) pseudocapacitance and (ii) electrical double-layer capacitance (EDLC) [2,13]. In general, conducting polymers and various metal oxides are employed as the active electrode materials in

pseudocapacitors, whereas EDLCs are based on nanostructured carbon materials, such as activated carbon (AC), carbon nanotubes, and graphene and its derivatives [14]. Alternatively, the construction of hybrid materials consisting of carbon and metal oxides has been studied as efficient materials to enhance the specific capacitance of the SCs [15].

Mixed transition metal oxides (MTMOs), due to their variable oxidation states, enable various redox processes and satisfactory structural properties are potential next-generation materials for high-performance SCs [15–17]. Further, carbon-based materials, such as rGO, carbon nanotubes, and activated carbon, have proven to be promising for hybrid materials, owing to their high surface area and good electrical conductivity. In recent years, much attention has been devoted to combining metal oxides with carbon-based materials that could further boost the electrochemical performance of SCs [8,11,18]. As electrodes in SCs, hybrid materials, especially with MTMOs, sometimes suffer from poor electrical conductivity and instability in contact with the electrolyte, which deteriorates the charge storage performance of the electrode. To overcome this drawback, noble metals, such as platinum [19], ruthenium [20], gold [21], or silver [22], in combination with nanomaterials, have gained attention as a way to improve the electrical conductivity on metal oxides. As a consequence of noble metal scarcity, the price of fabrication for these materials increases with increased loading. Therefore, the loading should be kept as low as possible.

Additionally, the fabrication technique is also important for the applicability of SC devices. State-of-the-art techniques for the synthesis of transition metal oxides and compositions include, but are not limited to, hydrothermal [7], chemical vapor deposition [23], spray pyrolysis [24], sol–gel [25], and electrodeposition [26]. Of all the techniques, the applicability of electrodeposition in the coating of the active material on the substrate has gained great interest due to its cost effectiveness, ease of scale-up, and facile operation [27,28].

Motivated by the advantages mentioned above, the present study aims to investigate the facile electrodeposition approach for the preparation of multiple-component mixed metal oxide, namely CoNi, MnCoNi, and Ag-doped MnCoNiO (Ag:MnCoNiO) deposited on rGO, and implementation as hybrid materials. These materials were tested as positive electrodes combined with activated carbon as a negative electrode in an asymmetric supercapacitor. All the electrochemical analysis is conducted in a 6 M KOH aqueous electrolyte solution. Structural and morphological properties were determined on Ag:MnCoNiO/rGO due to the highest displayed performance among all electrodes based on electrochemical analysis. Furthermore, the asymmetric supercapacitor (ASSC) performance of Ag:MnCoNiO/rGO as the positive electrode is further tested by assembling a device with AC as the negative electrode, exhibiting specific capacitance of 478.9 F/g at a scan rate of 5 mV s^{-1}.

2. Experimental

2.1. Materials

Graphite powder (<20 μm), nickel (II) acetate tetrahydrate ($(CH_3COO)_2$ Ni·$4H_2O$, 98%), cobalt (II) acetate tetrahydrate ($(CH_3COO)_2Co{\cdot}4H_2O$, 98%), manganese (II) acetate tetrahydrate ($(CH_3COO)_2Mn{\cdot}4H_2O$, ≥99%), sodium sulfate (Na_2SO_4, ≥99.0%), sulfuric acid (H_2SO_4, 96%), polyvinylidene difluoride (PVDF), hydrogen peroxide (H_2O_2, 30%), phosphoric acid (H_3PO_4, 85%), hydrochloric acid (HCl), charcoal-activated (particle size < 100 μm) carbon (99.95%), potassium hydroxide (KOH, ≥85%), potassium chloride (KCl, 99%), ethanol (CH_3CH_2OH, ≥99.9%), polyvinyl alcohol ($C_2H_2F_2$, Mw:145 kDa), N-methyl-2-pyrrolidone (C_5H_9NO, 99.5%), and silver nitrate ($AgNO_3$, 99.9999%) were purchased from Sigma Aldrich. All the chemicals were at an analytical grade and were used as received. Prior to the fabrication, the nickel foam (Goodfellow, Cambridgeshire, England, 1 cm × 1 cm) was cleaned ultrasonically with deionized water and 2 M HCl and acetone (each for 5 min) to remove the surface oxide layer from the substrate. The Mill-Q system (Merck Millipore, Darmstadt, Germany, Mill-Q IQ 7003, 18.2 MΩ) was used to prepare the ultrapure water used in all experiments.

2.2. Synthesis of Graphene Oxide (GO)

GO powder was synthesized using the improved Hummer's method [29]. The procedure was applied as follows, briefly: 1 g of pure graphite powders was firstly mixed with 30 mL concentrated H_2SO_4 and 3.3 mL H_3PO_4 in an ice bath and stirred for 30 min with a magnetic stirrer. Thereafter, 6 g $KMnO_4$ was slowly added to the above solution with magnetic stirring. The mixture was then heated at 35 °C and stirred for 2 h. Then, 100 mL of deionized (DI) water and 10 mL of H_2O_2 (30%) were dropped gradually into the solution with continuous stirring, which turned the color of the solution yellowish. The resulting mixture was separated by centrifugation. Ethanol and 5% HCl solution was used to wash the slurry followed by deionized water up to pH = 7. Lastly, the slurry was dried in a drying oven at 60 °C for 12h and ground into a brown powder to be used in characterization.

2.3. Synthesis of MTMO Electrodes

The synthesis procedure of Ag:MnCoNiO/rGO film on Ni foam was conducted in two parts: (i) rGO was fabricated on Ni foam by electrochemical reduction of GO. In this process, 1 g/L of GO was dissolved in 0.1 M KCl aqueous solution, stirred magnetically for 1 h, and then continued to shake ultrasonically for 1 h to homogenize the electrolyte. Before the fabrication, Ar gas was used for 10 min to purge dissolved oxygen from the electrolyte. Electrochemical reduction of GO on Ni foam was carried out by cyclic voltammetry in a potential range from −1.0 V to −1.4 V at a scan rate of 10 mV/s for 10 cycles. (ii) Ag-doped MnCoNiO film was synthesized by a facile electrodeposition method on rGO/Ni foam. In a typical preparation, 0.01 M nickel (II) acetate tetrahydrate, 0.01 M manganese (II) acetate tetrahydrate, 0.02 M cobalt (II) acetate tetrahydrate, 0.01 M sodium sulfate, and 0.5 mM silver nitrate were dissolved in DI water under vigorous stirring for 10 min to form a homogenous electrolyte before the fabrication. Regarding CoNiO synthesis, the electrolyte consisted of 0.02 M cobalt (II) acetate tetrahydrate, 0.01 M sodium sulfate, and 0.01 M nickel (II) acetate tetrahydrate. For the MnCoNiO preparation, 0.01 M manganese (II) acetate tetrahydrate was added to the above mixture. All the film depositions were performed by chronopotentiometry at a constant current density of -5 mA cm^{-2} for 30 min on rGO/Ni foam. At the end, the fabricated samples were washed with DI water, dried in an oven (Heraeus instruments, Hanau, Germany, Trockenschrank UT 612) at 60 °C, and annealed at 500 °C with 10 °C/min for 2 h in a tube furnace. The mass loading of Ag:MnCoNiO/rGO was measured by high-precision scale (Shimadzu, Kyoto, Japan, Advanced Performance Uniblocbalance) and was about 1.2 mg in all experiments.

2.4. Characterization

The structural properties of the samples were taken by X-ray diffraction (XRD) in a range between 10° and 90° using Bruker D8 advanced diffractometer apparatus equipped with CuKα radiation source (λ = 1.5418 Å). Scanning electron microscopy (SEM; Hitachi TM3030 PLUS, Tokyo, Japan) equipped with energy dispersive X-ray analysis (EDX) was used to analyze the morphology and elemental composition of the fabricated samples. The elemental composition was carried out by X-ray photoelectron spectroscopy (XPS, VersaProbe II, PHI, Japan). FT-IR spectra were taken by a Bruker Vertex 80 spectrometer in the 400–4000 cm^{-1} region.

2.5. Preparation of an All-Solid-State Supercapacitor and Electrochemical Analyses

The activated carbon electrode was fabricated by mixing activated carbon, binder (PVDF), and conductive carbon (80:10:10) in a mortar to make a slurry with N-methyl-2-pyrrolidone (NMP) solvent. The slurry was pasted on the Ni foam (1 cm × 1 cm) and dried at 60 °C in an oven for 12 h to be used as negative electrode. A gel electrolyte was prepared by dissolving 3 g of PVA and 3 g of KOH in 20 mL of DI water at 85 °C. After drying, in order to construct the ASSC device, the Ag:MnCoNiO on rGO/Ni foam was dipped in the gel electrolyte for 10 min.

The electrochemical measurements, such as cyclic voltammetry (CV), electrochemical impedance spectroscopy (EIS), and galvanostatic charge/discharge (GCD) were conducted by Bio-Logic VSP-3e (France) electrochemical workstation in a cell equipped with 99.99% platinum electrode as the counter electrode, Ag:MnCoNiO/rGO as a working electrode, and a mercury/mercurous sulphate (MMS) ($Hg/HgSO_4$) as the reference electrodes, respectively. A 6.0 M KOH solution was used for all tests. The CV with various scan rates and GCD under different current densities with a potential window range from 0.0 to +0.6 V was applied at room temperature. Electrochemical impedance spectroscopy (EIS) was carried out within a frequency range from 1 Hz to 100 kHz using an AC voltage with 10 mV amplitude at open-circuit potential. For the ASSC device, we developed an all-solid-state asymmetric supercapacitor (ASSC). In this configuration, Ag:MnCoNiO/rGO, as the best performing material, was used as the positive electrode and activated carbon was used as the corresponding negative electrode. Based on CV and GCD curves, the specific capacitance (C_S), energy density (E_c), and power density (P_c) can be evaluated by the equations given below [30,31]:

$$C_s = \frac{\int I\, dV}{mv\Delta V} \quad (1)$$

$$E_c = \frac{C_s \Delta V^2}{2 \times 3.6} \quad (2)$$

$$P_c = \frac{E_c \times 3600}{\Delta t} \quad (3)$$

where $\int I\, dV$ is the integrated area under CV curve, v is the scan rate, m is the mass of the active material in three-electrode system (total mass of both electrodes in the case of two-electrode system), Δt is the discharging time, and ΔV is the potential window.

3. Results and Discussion

3.1. Structural and Morphological Properties

In order to investigate the nature of the material, a structural analysis of Ag:MnCoNiO on rGO/Ni foam electrode was performed by XRD and the resulting diffraction pattern is depicted in Figure 1.

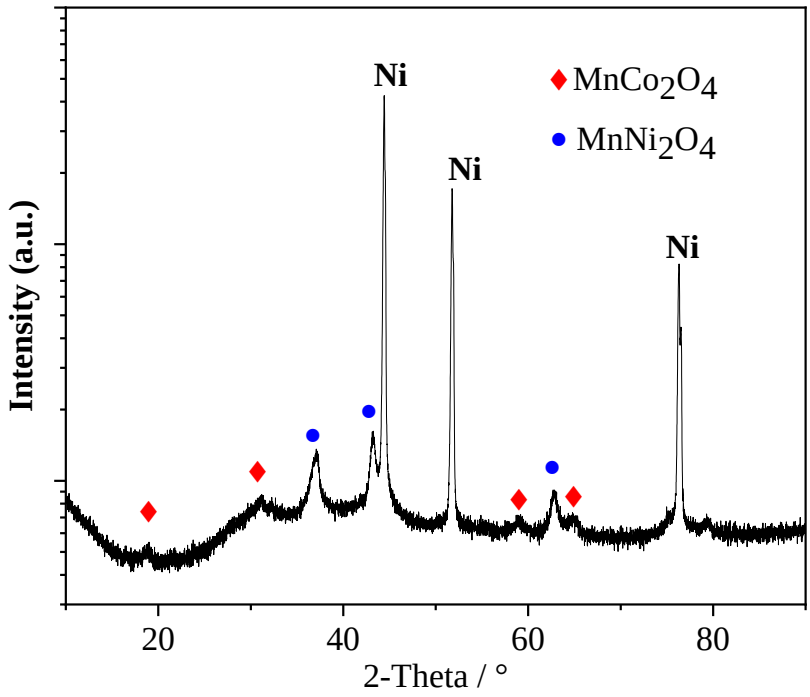

Figure 1. XRD pattern of the Ag:MnCoNiO on rGO/Ni foam electrode.

X-ray analysis displays the mixture of $MnCo_2O_4$ (JCPDS: 23-1237) and $MnNi_2O_4$ (JCPDS: 36-0083) phases [32]. However, there is a small shift observed in the XRD diffraction peaks according to these JCPDS cards due to the partial substitution of the Ag^+ ions by Mn^{2+} ions. A possible reason for this substitution could because Ag^+ ions (1.28 Å) have as larger ionic radius than Mn^{2+} (0.80 Å). The intense diffraction peaks obtained for the electrode, imply the poly-crystalline metal oxide nature. The peaks correspond to cubic $MnNi_2O_4$ spinel phase at 2θ = 18.9° (*hkl* = 111), 30.7° (*hkl* = 220), 58.8° (*hkl* = 511), and 63.1° (*hkl* = 440) with a lattice constant of a = b = c = 0.813 nm. The diffraction peaks at 2θ = 37.1°, 43.1°, and 62.3° for $MnCo_2O_4$ can be assigned to the (222), (400), and (440) lattice planes of cubic spinel structure, respectively. Also, the lattice parameters a, b, and c for $MnCo_2O_4$ is 0.831 nm. There were no reflection peaks related to any impurities. In addition, no peaks associated with Ag were detected due to its low loading (while it appears in XPS), proving that Ag was successfully doped into the mixed metal oxide. The XRD result confirms the crystalline nature of the material.

The surface elemental compositions and oxidation state of the Ag:MnCoNiO/rGO electrode were analyzed by X-ray photon spectroscopy (XPS), using a Gaussian fitting model. Figure 2a–g depicts the corresponding spectra of Ni 2p, Mn 2p, Co 2p, C 1s, O 1s, and Ag 3d, respectively.

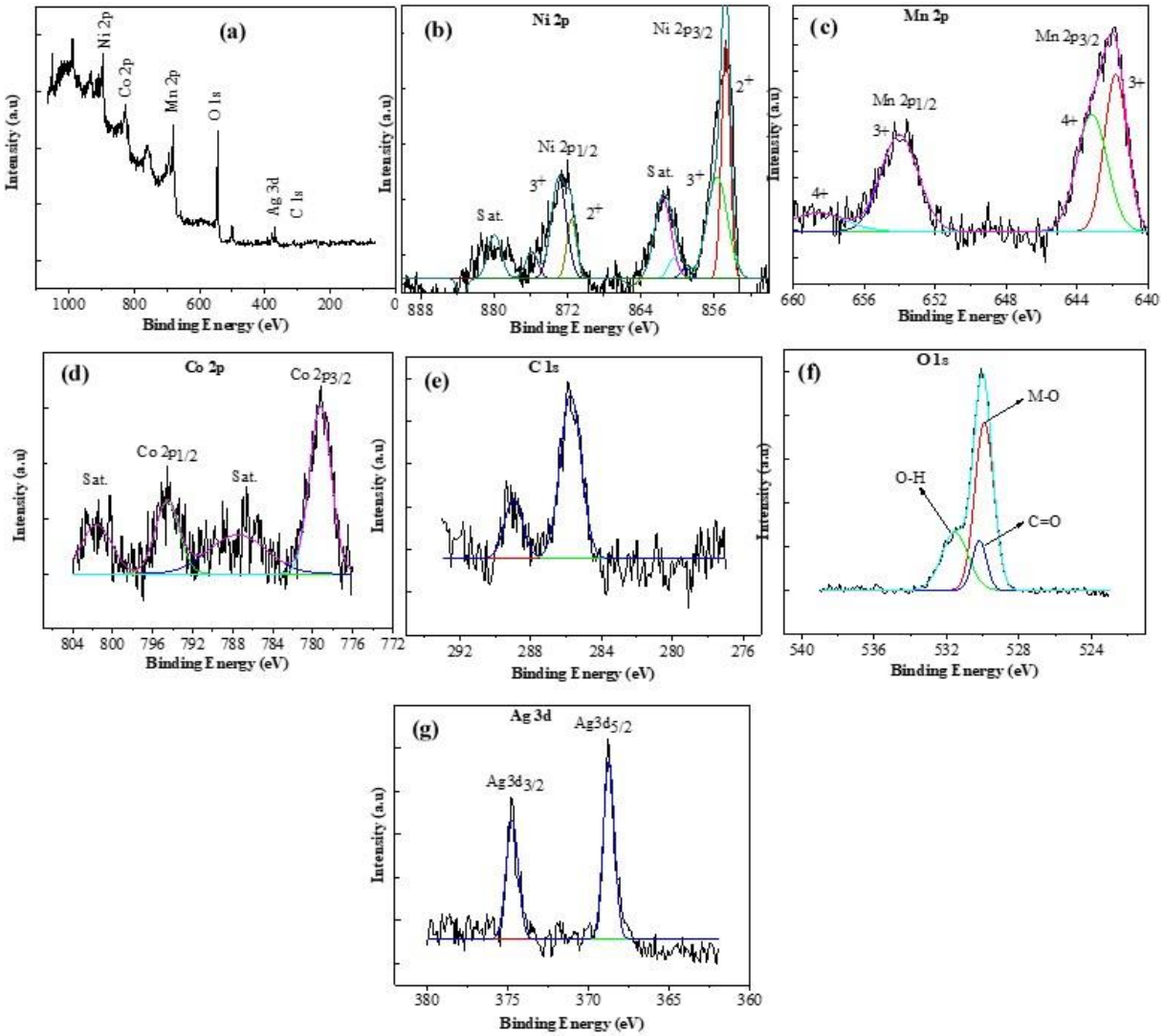

Figure 2. XPS profile of Ag:MnCoNiO/rGO electrode (**a**) survey spectrum (**b**) Ni 2p, (**c**) Mn 2p, (**d**) Co 2p, (**e**) C 1s, (**f**) O 1s, and (**g**) Ag 3d.

Figure 2a shows the survey spectrum for the fabricated electrode, which reveals the presence of Ni 2p, Mn 2p, Co 2p, C 1s, O 1s, and Ag 3d, consistent with EDX analysis (Figure 4). The XPS spectrum of Ni (Figure 2b) shows doublet peaks positioned at 872.5 eV and 854.7 eV, which are assigned to Ni $2p_{1/2}$ and Ni $2p_{3//2}$, respectively, and it also displays multiple splitting with two satellite peaks of Ni 2p 880.2 and 861.6 eV. The corresponding satellite peaks of Ni 2p indicate the presence of a spin-orbital region of NiO [33]. Figure 2c depicts the binding energies of 642and 654 eV, which are attributed to Mn $2p_{3/2}$ and Mn $2p_{1/2}$ split orbital, respectively [26]. The XPS spectra of Co 2p (Figure 2d) demonstrates two pairs of peaks positioned at 779.3 and 794.5 eV, related to the characteristic spin-orbit doublets of Co $2p_{1/2}$ and Co $2p_{3/2}$, respectively. In addition, there are two shakeup satellite (sat.) peaks at 801.5 and 786.8 eV, which are characteristic lines of high-spin Co^{2+} [34]. The peak for C 1s XPS spectra (Figure 2e), located at around 285.5 eV, is assigned to C-C, C=C and C-H bonds. The binding energy of 289.3 eV can be assigned to C-OH, C=O, and O=C-OH functional groups [35]. The deconvoluted O 1s XPS spectrum (Figure 2f) displays three peaks located at 529.8, 530.2, and 531.5 eV, which are representative of Co/Mn/Ni-oxygen bonding, C=O, and O-H, respectively [13,32]. Figure 2g shows the XPS spectrum of Ag 3d doublets with binding energies located at 374.8 and 368.8 eV, which are ascribed to the Ag $3d_{3/2}$ and Ag $3d_{5/2}$ transitions [36]. This is in good agreement with the work conducted by Potlog et al., who reported that the appearance of these peaks is related to the metallic silver (Ag^0) [37]. The XPS analysis further indicates the successful fabrication of Ag:MnCoNiO/rGO, which is supported by XRD and EDX.

The FT-IR technique was used to find the characteristic functional bonds in an electrode. Figure 3a depicts the FT-IR spectra of the GO, rGO, and Ag:MnCoNiO materials in a range between 400 and 4000 cm^{-1}. Regarding GO powder, the presence of the wide band nearly at 3200 cm^{-1} comes from O-H stretching vibration and physically adsorbed water molecules [38,39]. The other three characteristic absorption bands are indicative features of the GO, which are located at 1047 cm^{-1} (C-O), 1634 cm^{-1} (C=C), and 1733 cm^{-1} (C=O) [40,41]. After electrochemical reduction of the GO, most of the oxygen-containing functional bands, such as hydroxyl groups (O-H), are not visible in the FT-IR spectra of the rGO. For the Ag:MnCoNiO electrode, the strong and sharp signal around 600 cm^{-1} might be related to the stretching vibration of the metal–oxygen bond (Mn,Co,Ni-O) [42,43].

A scanning electron microscope (SEM) image of Ag:MnCoNiO on rGO/Ni foam electrode is shown in Figure 3b. From the high-magnification image, it shows that the sample has densely packed clusters with some cracks throughout the whole substrate. These cracks could be beneficial, since they can provide easier accessibility of K^+ ions for enhancing specific capacitance [44]. The EDX spectrum of Ag:MnCoNiO on rGO/Ni is shown in Figure 4a, which confirms the presence of Mn, Co, Ni, O, and Ag, revealing the successful formation of Ag:MnCoNiO on rGO/Ni foam electrode and successful Ag doping. The atomic percentage of the electrode comprises 44.11% O, 2.31% S, 17.35% Co, 31.17% Ni, 1.67% Mn, 2.46% Na, 0.72% Ag, and 0.19% Cl. The elemental EDX mapping of Ag:MnCoNiO is shown in Figure 4b and it confirms the homogenous distribution of Mn, Co, Ni, O, and Ag elements on the rGO/Ni foam surface.

3.2. Electrochemical Characterization

In order to explore the significance of the components in the hybrid electrodes and the effects of the mixed metal oxides and compare their electrochemical behavior, a series of samples were tested: (1) bare Ni foam, (2) rGO on Ni foam, as well as (3) CoNiO, (4) MnCoNiO, and (5) Ag:MnCoNiO on rGO/Ni foam electrodes. All samples were tested with electrochemical techniques, such as cyclic voltammetry (CV), galvanostatic charge–discharge (GCD), and electrochemical impedance spectroscopy (EIS), in a three-electrode cell configuration in 6 M KOH aqueous electrolyte.

A CV comparison of the produced samples is depicted in Figure 5a, which was obtained at a scan rate of 100 mV s^{-1} in a potential range between 0.0 and +0.6 V.

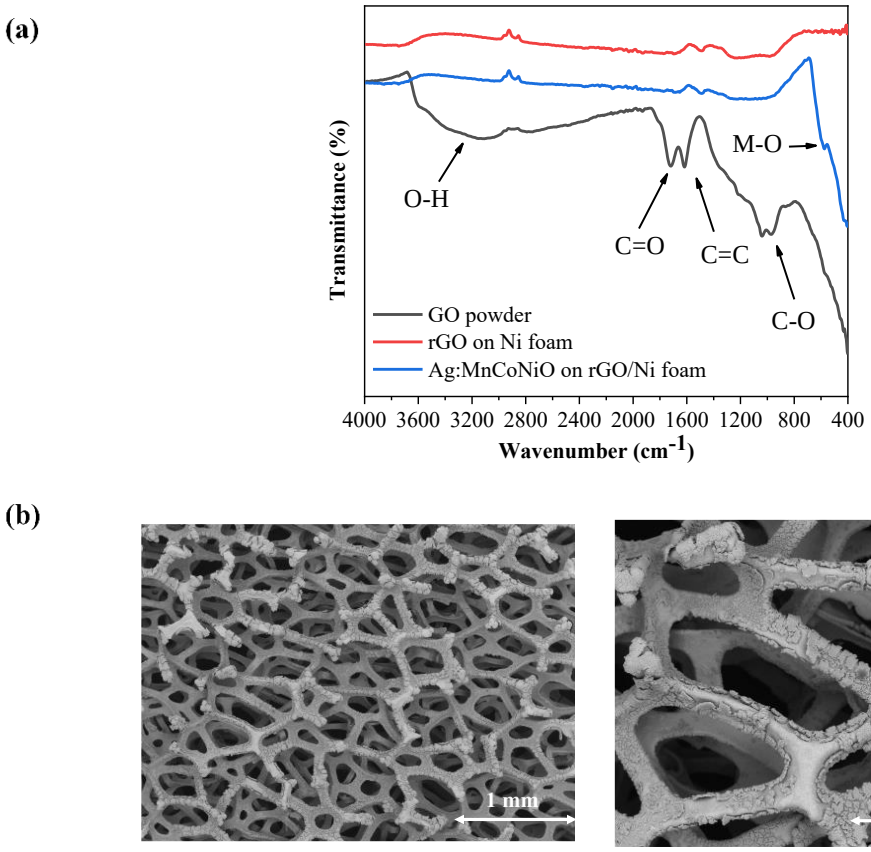

Figure 3. (**a**) FT-IR spectra of GO powder, rGO on Ni foam, and Ag:MnCoNiO on rGO/Ni foam (**b**) SEM images of the Ag:MnCoNiO on rGO/Ni foam electrode.

As can be clearly seen from Figure 5a, all the electrodes have broad oxidation waves in the anodic and a reduction wave in the cathodic scan. The presence of these peaks indicates the pseudocapacitive nature of the electrode material, which is dominated by Faradic redox reactions [2,45]. Compared to other electrodes, bare Ni foam has a very small integral area in the CV curve; hence, the specific capacitance contribution from the substrate can be neglected. It can be clearly seen from Figure 5a that from the CV profiles of five samples, the maximum integrated area under the CV curve is observed for the Ag:MnCoNiO on rGO/Ni foam, suggesting that it has the most pronounced (pseudo)capacitive behavior, owing to the improved conductivity by Ag doping. Additionally, Ag:MnCoNiO on rGO/Ni foam has the highest current density compared to all electrodes tested, indicating a fast redox reaction process. Moreover, the redox peaks of MnCoNiO are significantly larger compared with the CoNiO, indicating that the contribution of the Mn and each individual element is significant. Figure 5b illustrates the corresponding comparison of GCD curves for fabricated electrodes measured in the same potential range at a current density of 1 A/g. As can be seen clearly from Figure 5b, the GCD curves at a current density of 1 A/g for all the fabricated materials display typical charge–discharge curve shapes, suggesting that the capacitive contribution of these samples is generally due to the faradic reactions occurring at the electrode surface [46]. Apparently, all the samples show GCD curves approximately symmetrical and nonlinear in shape, revealing the good reversibility and high coulombic efficiency of the material. The Ag:MnCoNiO on the rGO/Ni foam electrode has the longest discharge time compared to the other electrodes, which indicates that this electrode has a better specific capacitance out of all the electrodes tested in this work. This result is also in agreement with the CV results. The discharging times are decreasing with current density, signifying that a high current density shortens the necessary time required for ions to migrate into the electrode [47]. Figure 5c shows a typical CV curve for Ag:MnCoNiO on the rGO/Ni foam electrode with various scan rates from 5 to 100 mV s^{-1}.

There is no change in the shape of the CV curves for each scan rate, but a shift in the peak locations in the CV curves can be seen with the increase in scan rates. This shift can be explained by the polarization of the electrolyte at higher scan rates [13,48]. As shown in CVs in Figure 5c, there is a broad reduction peak positioned at +0.3 V, which is ascribed to the reduction of mixed metal oxides (M^{+4}/M^{+3} to M^{+2} and M^{+2} to M^{0}). In the reverse scan, there are two peaks located at +0.2 and +0.1 V, signifying oxidation of mixed metal oxides (M^{0} to M^{+2} and further M^{+2} to M^{+4}/M^{+3}) [49]. Similar CV behavior was also observed in the work conducted by Singh et al. [50]. The specific capacitance values for the Ag:MnCoNiO on the rGO/Ni foam electrode are calculated by Eq. 1 and found to be 280.3, 329.8, 378.7, 413.3, and 441.7 F/g at scan rates of 100, 50, 20, 10, and 5 mV/s, respectively. Compared to previous studies, the calculated specific capacitances for the fabricated electrode are comparable. Talluri et al. [6] synthesized $(CoCrFeMnNi)_3O_4$ via a reverse co-precipitation process and they reported specific capacitance 239 F g^{-1} at 0.5 A g^{-1} from GCD curves. Further, as the scan rate increases, the specific capacitance values decrease. Such a significant decrease in capacitance with increasing scan rate is likely to be caused by the drop in accessibility of the K^{+} ions in the solution, which cannot diffuse deep into the active sites of the electrode at higher scan rates [6].

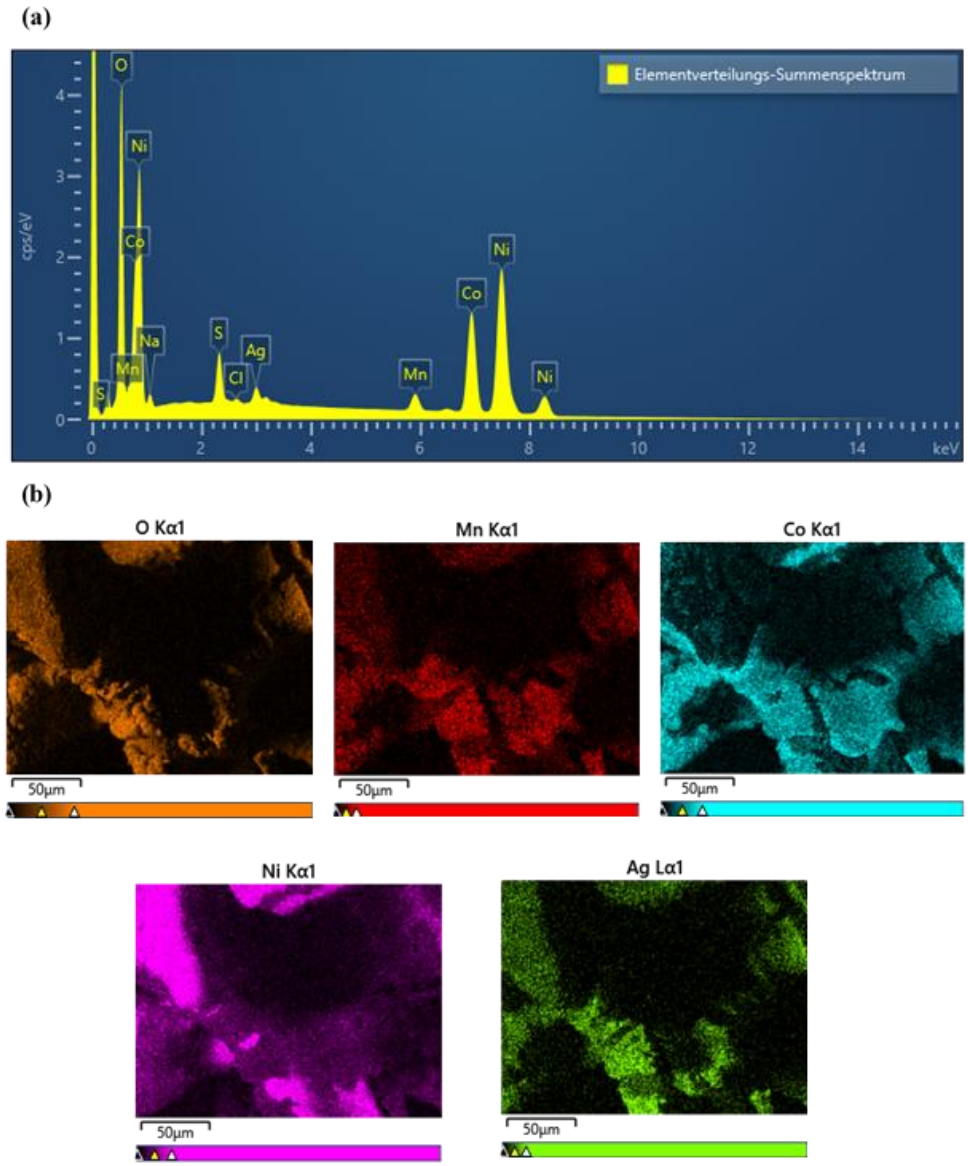

Figure 4. (**a**) EDX spectrum and (**b**) elemental EDX mapping of Ag:MnCoNiO on rGO/Ni foam electrode.

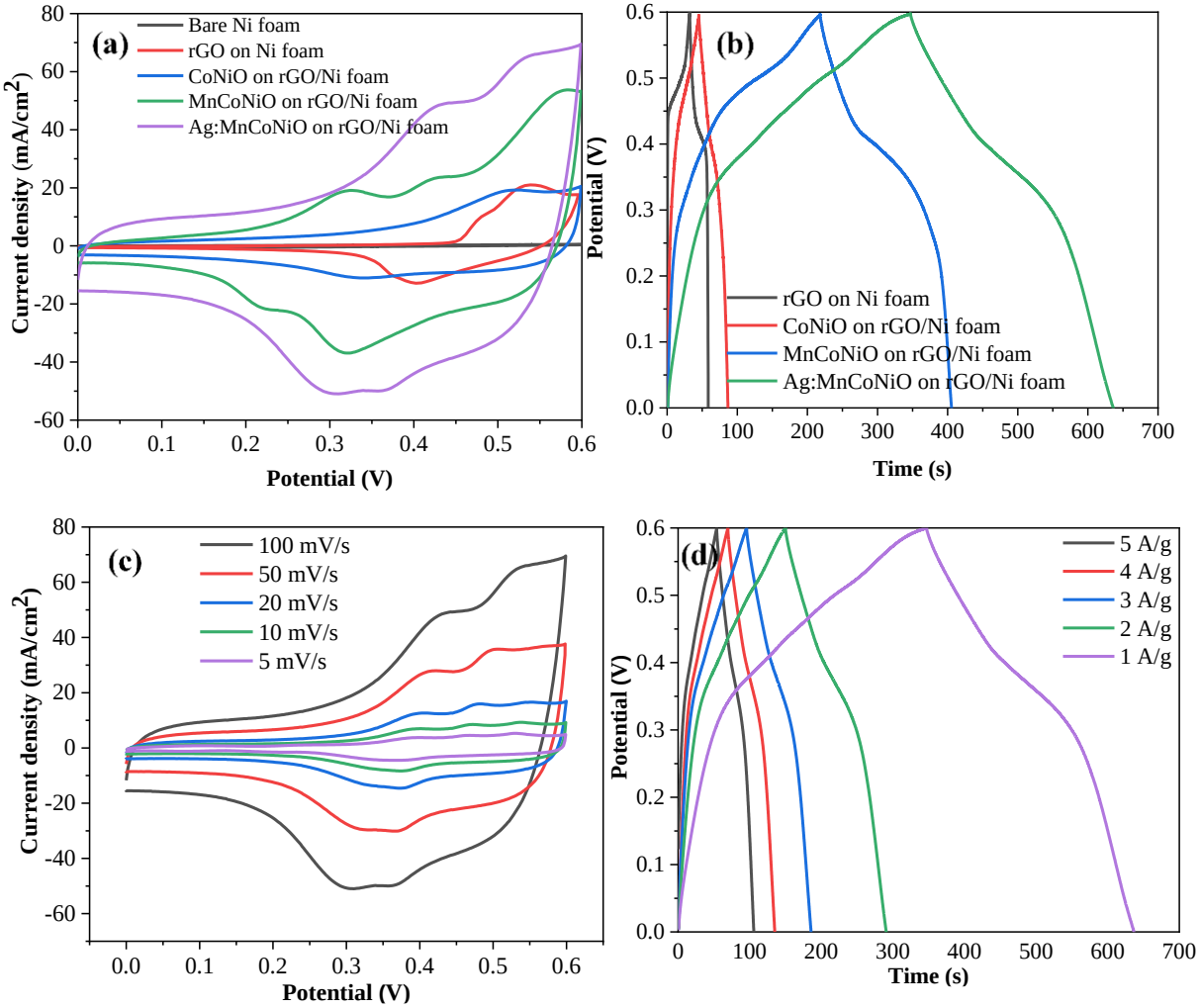

Figure 5. Comparison of electrochemical properties of Ni foam, rGO on Ni foam, CoNiO, MnCoNiO, and Ag:MnCoNiO on rGO/Ni foam electrodes. (**a**) CV curves with a scan rate of 100 mV/s, (**b**) GCD curves at a current density of 1 A/g, (**c**) CV curves of Ag:MnCoNiO with different scan rate, and (**d**) GCD curves of Ag:MnCoNiO with different current densities.

3.3. Electrochemical Performance of All-Solid-State ASSC Device

To test further practical application, we attempted to construct an ASSC device with Ag:MnCoNiO on the rGO/Ni foam as the positive electrode and AC on Ni foam as the negative electrode (Figure 6).

Before device construction, a comparison of the CV results for both the positive and negative electrode in a three-electrode system at a scan rate of 100 mV s^{-1} is depicted in Figure 7a.

Figure 7b depicts the CV curve of the constructed ASSC device at 100 mV s^{-1}, with a different potential window, verifying that the device could function suitably up to 1.8 V. The specific capacitance variations with respect to the scan rate and the inset show a series of CV curves for the ASSC device under various scan rates 5–100 mV s^{-1} at a potential range of 0.0 V and 1.8 V, shown in Figure 7c. It can be seen that no obvious deformation of the CV curves is visible and the reduction peak progressively shifted to a lower potential when the scan rate increased. This shift can be attributed to the polarization of the electrolyte [13]. From the CV curves, the specific capacitance values of the device are found to be 161.5, 210, 286.9, 389.3, and 478.9 F/g at scan rates of 100, 50, 20, 10, and 5 mV/s, respectively. Figure 7d displays the GCD curves of the ASSC device under different current densities within a potential range of 0–1.8 V. The observed quasi-symmetrical curves have long discharging times, revealing a good capacitive be-

havior and good electrochemical reversibility. The specific capacitance decreases with increasing current density, which may be due to the decrease in mobility of the ions in the electrolyte into the inner surface of the electrode material [51]. The energy density and power density were calculated with Equations (2) and (3) for two-electrode systems. The device provided a maximum energy density of 45.5 Wh/kg and possessed maximum power density of 4500 W/kg. It can be seen from Figure 7e that the cyclic stability of the assembled ASSC device retains 86% of the coulombic efficiency at 5 A/g over 5000 cycles, which further confirms high charge–discharge reversibility of the ASSC device. A literature review is listed in Table 1, showing an overview of device performance of mixed metal oxide supercapacitors. For example, Zhang et al. [52] fabricated $Co_{0.5}Mn_{0.4}Ni_{0.1}C_2O_4{*}H_2O$ electrodes via a room temperature chemical co-precipitation method and they found 0.46 mWh cm^{-3} and capacitance retention of 98.6% after 6000 cycles. Talluri et al. [6] prepared $(CoCrFeMnNi)_3O_4$ electrode using a reverse co-precipitation approach and, according to their findings, the electrode provides 24.1 Wh kg^{-1} at a current density of 0.5 A g^{-1}. Biswal et al. [53] synthesized a cobalt–nickel–copper ternary metal oxide via electrochemical deposition followed by calcination and the device exhibited 188 F g^{-1} at a current density of 0.1 A g^{-1} and 95.1% capacitance retention after 1000 cycles. This short literature review shows that the MTMO-based supercapacitor shows comparable properties, while being fabricated in a simple, electrochemical deposition method, without any additional surface structuring.

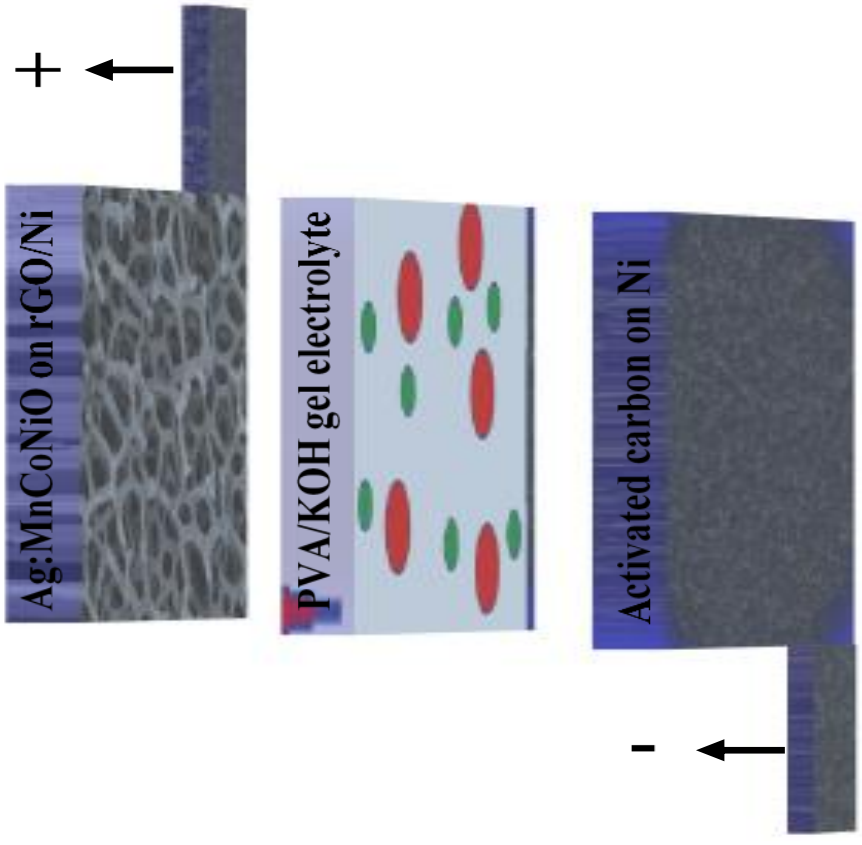

Figure 6. Schematic diagram of the assembled all-solid-state AC//Ag:MnCoNiO device.

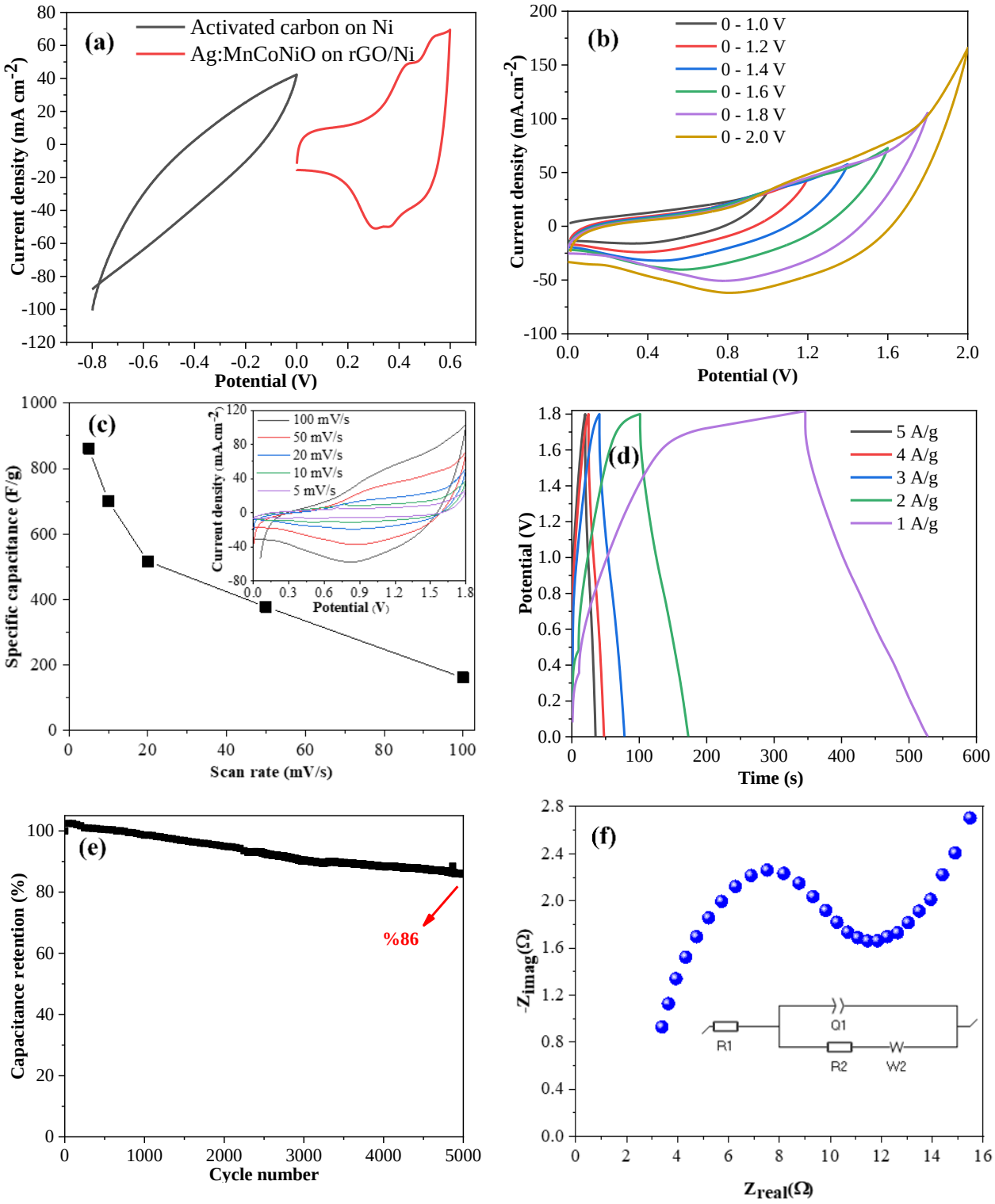

Figure 7. Electrochemical performance of the AC//Ag:MnCoNiO devices. (**a**) CV comparison at 100 mV s^{-1} in three-electrode system: (**b**) CV curves at different potential windows; (**c**) CV curves at different scan rates; (**d**) GCD curves at different current densities; (**e**) cyclic stability at 5 A g^{-1}; (**f**) Nyquist diagram.

Table 1. Performance comparison of Ag:MnCoNiO//AC device with other studies.

Electrode Material	Specific Capacitance	Retention	Energy Density	Power Density	Ref.
$Co_{0.5}Mn_{0.4}Ni_{0.1}C_2O_4*nH_2O$//Graphene	990 Fg^{-1} at 0.6 Ag^{-1}	98.6% 6000 cycle	0.46 mWh cm^{-3}	46 mW cm^{-3}	[52]
Co_3O_4-MnO_2-NiO	2525 F g^{-1}	88% 5700 cycle	108.8 Wh kg^{-1}	8 kW kg^{-1}	[50]
$MnCo_2O_{4.5}$@$NiCo_2O_4$	325 F g^{-1} at 1 Ag^{-1}	70.5% 3000 cycle	-	-	[54]
P-$NiCo_2O_4$/$NiMoO_4$//AC	2334 F g^{-1} at 1 Ag^{-1}	89.97% 8000 cycle	45.1 Wh kg^{-1}	800 W kg^{-1}	[55]
$(CoCrFeMnNi)_3O_4$	239 F g^{-1} at 0.5 Ag^{-1}	86% 1000 cycle	24.1 Wh kg^{-1}	-	[6]
$MnCo_2O_4$@$Ni(OH)_2$	2514 F g^{-1} at 5 Ag^{-1}	90% 2500 cycle	48 Wh kg^{-1}	14.9 kW kg^{-1}	[56]
$MnCo_2O_4$/Ni-MOF	957.11 F g^{-1} at 1 Ag^{-1}	83.33% 16,000 cycle	35.6 Wh kg^{-1}	749.91 W kg^{-1}	[57]
$NiMn_2O_4$	571 F g^{-1} at 5 mVs^{-1}	96% 2000 cycle	11.9 Wh kg^{-1}	44.4 kW kg^{-1}	[58]
Co-Ni-Cu mixed oxide	188 F g^{-1} at 0.1 Ag^{-1}	95% 1000 cycle	61.6 Wh kg^{-1}	1.5 kW kg^{-1}	[53]
$Ni_xCo_yMo_zO$	126 mF cm^{-2}	-	22.02 Wh kg^{-1}	3.5 W kg^{-1}	[59]
$NiCo_2O_4$/$ZnCo_2O_4$@rGO/CNTs	143 F g^{-1} at 1 Ag^{-1}	86.1% 9000 cycle	50.8 Wh kg^{-1}	800 W kg^{-1}	[60]
$Mg_{0.1}Mn_{0.9}Fe_2O_4$	226.4 F g^{-1} at 0.5Ag^{-1}	94.5% 3000 cycle	-	-	[61]
Ag:MnCoNiO//AC	478.9 F g^{-1} at 5 mVs^{-1}	86% 6000 cycle	45.5 Wh kg^{-1}	4.5 kW kg^{-1}	This work

Additionally, the internal resistances of the device were also investigated by performing EIS tests (Figure 7f). The data were fitted using EC-lab software to the equivalent electric circuit shown at the inset. It can be observed that the spectra have two different components: (a) a semi-circle in the high-frequency region and (b) a straight line in the low-frequency region. The circumference of the semi-circle at high frequency is indicative of charge-transfer resistance (R_{CT}), correlated with the Faradic reactions of the device involved in the insertion/extraction of K^+ ions [62]. The straight line at low frequency is attributed to Warburg impedance, which refers to the diffusion resistance of K^+ ions into the material [63]. The evaluated value of the solution resistance (R_S), the charge–transfer resistance (R_{CT}), Warburg impedance (W_2), and capacitance (Q_1) of the device were found to be 2.1 Ω, 10.9 Ω, 7.243 ohm.$s^{-1/2}$, and 1.434.10^{-3} F, respectively.

4. Conclusions

In conclusion, CoNi, MnCoNi, and Ag-doped MnCoNiO MTMOs were grown on rGO/Ni foam and characterized by electrochemical and surface science methods. An all-solid-state ASSC device was further assembled by using the best performing Ag:MnCoNiO on rGO/Ni foam as the positive electrode and AC as the negative electrode. The SEM investigations reveal the uniform distribution of MnCoNiO on rGO/Ni foam. XRD, XPS, FT-IR, and EDX characterizations support the formation of the Ag:MnCoNiO on rGO/Ni foam. In a three-electrode setup, the fabricated electrode showed a specific capacitance of 441.5 F/g at scan rate of 5 mV s^{-1}. In the two-electrode setup, the device exhibited an energy density of 45.5 Wh kg^{-1} and retained 86%. These values are also comparable with other non-structured metal-oxide-based supercapacitors. Furthermore, the experiments showed that the synergistic contribution of all the constituents gives rise to the behavior of the mixed metal oxide, not directly predictable from the individual constituents, and that leaving out one element changes the properties significantly.

Author Contributions: Field data collection, analysis, and original draft preparation: Y.E.F.; writing—review, proof reading, and editing: V.Č. All authors have read and agreed to the published version of the manuscript.

Funding: This research received no external funding.

Data Availability Statement: The data presented in the study are available on request from the corresponding author.

Acknowledgments: Y.E.F. was supported by the Scientific and Technological Research Council of Turkey (TUBITAK) 2219-International Postdoctoral Research Fellowship Program 1059B192001238. Further, Y.E.F. and V.Č. acknowledge the Max Planck Institute for Chemical Energy Conversion for funding part of this work.

Conflicts of Interest: The authors declare no conflict of interest.

References

1. Xie, A.; Wang, H.; Zhu, Z.; Zhang, W.; Li, X.; Wang, Q.; Luo, S. Mesoporous CeO_2-α-MnO_2-Reduced Graphene Oxide Composite with Ultra-High Stability as a Novel Electrode Material for Supercapacitor. *Surf. Interfaces* **2021**, *25*, 101177. [CrossRef]
2. Zhao, L.; Lei, S.; Tu, Q.; Rao, L.; Zen, W.; Xiao, Y.; Cheng, B. Phase-Controlled Growth of Nickel Hydroxide Nanostructures on Nickel Foam for Enhanced Supercapacitor Performance. *J. Energy Storage* **2021**, *43*, 103171. [CrossRef]
3. Parale, V.G.; Kim, T.; Patil, A.M.; Phadtare, V.D.; Choi, H.; Dhavale, R.P.; Kim, Y.; Jun, S.C.; Park, H.H. Construction of Hierarchical Nickel Cobalt Sulfide@manganese Oxide Nanoarrays@nanosheets Core-Shell Electrodes for High-Performance Electrochemical Asymmetric Supercapacitor. *Int. J. Energy Res.* **2022**, *46*, 5250–5259. [CrossRef]
4. BoopathiRaja, R.; Vadivel, S.; Parthibavarman, M.; Prabhu, S.; Ramesh, R. Effect of Polypyrrole Incorporated Sun Flower like $Mn_2P_2O_7$ with Lab Waste Tissue Paper Derived Activated Carbon for Asymmetric Supercapacitor Applications. *Surf. Interfaces* **2021**, *26*, 101409. [CrossRef]
5. Li, Y.; Jiang, H.; Yan, X.; Zhang, W.; Zhang, M.; Zhu, W.; Pan, J.; Javed, M.S.; Cheng, W.; Guan, Y. Rationally Designed Mn_2O_3/Cu_xO Core–Shell Heterostructure Generated on Copper Foam as Binder-Free Electrode for Flexible Asymmetric Supercapacitor. *Appl. Surf. Sci.* **2021**, *566*, 150715. [CrossRef]
6. Talluri, B.; Aparna, M.L.; Sreenivasulu, N.; Bhattacharya, S.S.; Thomas, T. High Entropy Spinel Metal Oxide $(CoCrFeMnNi)_3O_4$ Nanoparticles as a High-Performance Supercapacitor Electrode Material. *J. Energy Storage* **2021**, *42*, 103004. [CrossRef]
7. Mani, M.P.; Venkatachalam, V.; Thamizharasan, K.; Jothibas, M. Evaluation of Cubic-Like Advanced ZnMn2O4 Electrode for High-Performance Supercapacitor Applications. *J. Electron. Mater.* **2021**, *50*, 4381–4387. [CrossRef]
8. Muthu, D.; Vargheese, S.; Haldorai, Y.; Kumar, R.T.R. NiMoO4/Reduced Graphene Oxide Composite as an Electrode Material for Hybrid Supercapacitor. *Mater. Sci. Semicond. Process.* **2021**, *135*, 106078. [CrossRef]
9. Wang, J.; Wang, C.; Wang, S.; Zhang, X.; Jin, X.; Chang, J.; Dong, J. A Porous ZnCo2O4 Nanosheets Arrays as a Binder-Free Electrode for High-Performance Flexible Supercapacitor Materials. *J. Mater. Sci. Mater. Electron.* **2021**, *32*, 25247–25257. [CrossRef]
10. Yan, J.; Li, S.; Lan, B.; Wu, Y.; Lee, P.S. Rational Design of Nanostructured Electrode Materials toward Multifunctional Supercapacitors. *Adv. Funct. Mater.* **2020**, *30*, 1902564. [CrossRef]
11. Liu, H.; Zhang, M.; Song, Z.; Ma, T.; Huang, Z.; Wang, A.; Shao, S. A Super Hybrid Supercapacitor with High Energy Density Based on the Construction of CoMoO4/MoO2 Decorated 3D Sulfur-Doped Graphene and Porous Lotus Leaves Carbon. *J. Alloys Compd.* **2021**, *881*, 160660. [CrossRef]
12. Ahmad, M.W.; Anand, S.; Fatima, A.; Yang, D.J.; Choudhury, A. Facile Synthesis of Copper Oxide Nanoparticles-Decorated Polyaniline Nanofibers with Enhanced Electrochemical Performance as Supercapacitor Electrode. *Polym. Adv. Technol.* **2021**, *32*, 4070–4081. [CrossRef]
13. Xu, Z.; Gao, R.; Yang, T.; Hou, X.; Cao, L. Three-Dimensional $NiCo_2O_4$ Nanosheets Arrays on Carbon Nanofibers for High-Performance Asymmetric Solid-State Supercapacitor. *Diam. Relat. Mater.* **2021**, *119*, 108584. [CrossRef]
14. Makkar, P.; Ghosh, N.N. High-Performance All-Solid-State Flexible Asymmetric Supercapacitor Device Based on a Ag-Ni Nanoparticle-Decorated Reduced Graphene Oxide Nanocomposite as an Advanced Cathode Material. *Ind. Eng. Chem. Res.* **2021**, *60*, 1666–1674. [CrossRef]
15. Wang, Z.; Wang, D.; Lu, Z.; Liu, J.; Xuan, D.; Liu, Q.; Chen, M.; Luo, F.; Li, S.; Zheng, Z. Battery-Type $MnCo_2O_4$@carbon Nanofibers Composites with Mesoporous Structure for High Performance Asymmetric Supercapacitor. *Diam. Relat. Mater.* **2021**, *119*, 108586. [CrossRef]
16. Wu, W.; Zhao, C.; Wang, C.; Liu, T.; Wang, L.; Zhu, J. Hierarchical Structure of Self-Supported NiCo2S4 Nanoflowers@$NiCo_2S_4$ Nanosheets as High Rate-Capability and Cycling-Stability Electrodes for Advanced Supercapacitor. *Appl. Surf. Sci.* **2021**, *563*, 150324. [CrossRef]
17. Beknalkar, S.A.; Teli, A.M.; Harale, N.S.; Pawar, K.K.; Patil, D.S.; Shin, J.C.; Patil, P.S. Hierarchical ITO Nanofibers Coated Mn_3O_4 Nanoplates Core-Shell Nanocomposites for High Performance All-Solid-State Symmetric Supercapacitor Device. *Ceram. Int.* **2021**, *47*, 29771–29785. [CrossRef]
18. Shinde, S.K.; Karade, S.S.; Maile, N.C.; Yadav, H.M.; Ghodake, G.S.; Jagadale, A.D.; Jalak, M.B.; Lee, D.S.; Kim, D.Y. Synthesis of 3D Nanoflower-like Mesoporous NiCo2O4 N-Doped CNTs Nanocomposite for Solid-State Hybrid Supercapacitor; Efficient Material for the Positive Electrode. *Ceram. Int.* **2021**, *47*, 31650–31665. [CrossRef]
19. Tamaekong, N.; Liewhiran, C.; Wisitsoraat, A.; Phanichphant, S. Sensing Characteristics of Flame-Spray-Made Pt/ZnO Thick Films as H2 Gas Sensor. *Sensors* **2009**, *9*, 6652–6669. [CrossRef]
20. Wang, C.; Shang, H.; Li, J.; Wang, Y.; Xu, H.; Wang, C.; Guo, J.; Du, Y. Ultralow Ru Doping Induced Interface Engineering in MOF Derived Ruthenium-Cobalt Oxide Hollow Nanobox for Efficient Water Oxidation Electrocatalysis. *Chem. Eng. J.* **2021**, *420*, 129805. [CrossRef]
21. Iliev, V.; Tomova, D.; Bilyarska, L. Promoting the Oxidative Removal Rate of 2,4-Dichlorophenoxyacetic Acid on Gold-Doped WO_3/TiO_2/Reduced Graphene Oxide Photocatalysts under UV Light Irradiation. *J. Photochem. Photobiol. A Chem.* **2018**, *351*, 69–77. [CrossRef]
22. Sawangphruk, M.; Pinitsoontorn, S.; Limtrakul, J. Surfactant-Assisted Electrodeposition and Improved Electrochemical Capacitance of Silver-Doped Manganese Oxide Pseudocapacitor Electrodes. *J. Solid State Electrochem.* **2012**, *16*, 2623–2629. [CrossRef]

23. Bai, X.L.; Gao, Y.L.; Gao, Z.Y.; Ma, J.Y.; Tong, X.L.; Sun, H.B.; Wang, J.A. Supercapacitor Performance of 3D-Graphene/MnO_2foam Synthesized via the Combination of Chemical Vapor Deposition with Hydrothermal Method. *Appl. Phys. Lett.* **2020**, *117*, 183901. [CrossRef]
24. Deokate, R.J.; Kalubarme, R.S.; Park, C.J.; Lokhande, C.D. Simple Synthesis of $NiCo_2O_4$ Thin Films Using Spray Pyrolysis for Electrochemical Supercapacitor Application: A Novel Approach. *Electrochim. Acta* **2017**, *224*, 378–385. [CrossRef]
25. Lin, C.K.; Chuang, K.H.; Lin, C.Y.; Tsay, C.Y.; Chen, C.Y. Manganese Oxide Films Prepared by Sol-Gel Process for Supercapacitor Application. *Surf. Coatings Technol.* **2007**, *202*, 1272–1276. [CrossRef]
26. Allado, K.; Liu, M.; Jayapalan, A.; Arvapalli, D.; Nowlin, K.; Wei, J. Binary MnO_2/Co_3O_4 metal Oxides Wrapped on Superaligned Electrospun Carbon Nanofibers as Binder Free Supercapacitor Electrodes. *Energy Fuels* **2021**, *35*, 8396–8405. [CrossRef]
27. Muzakir, M.M.; Zainal, Z.; Lim, H.N.; Abdullah, A.H.; Bahrudin, N.N. Enhanced Capacitive Performance of Cathodically Reduced Titania Nanotubes Pulsed Deposited with Mn2O3as Supercapacitor Electrode. *RSC Adv.* **2021**, *11*, 26700–26709. [CrossRef]
28. Dharmadasa, I.M.; Haigh, J. Strengths and Advantages of Electrodeposition as a Semiconductor Growth Technique for Applications in Macroelectronic Devices. *J. Electrochem. Soc.* **2006**, *153*, G47. [CrossRef]
29. Das, P.; Deoghare, A.B.; Maity, S.R. A Novel Approach to Synthesize Reduced Graphene Oxide (RGO) at Low Thermal Conditions. *Arab. J. Sci. Eng.* **2021**, *46*, 5467–5475. [CrossRef]
30. Heiba, Z.K.; Deyab, M.A.; Mohamed, M.B.; Farag, N.M.; El-naggar, A.M.; Plaisier, J.R. Electrochemical Performance of CuCo2O4/CuS Nanocomposite as a Novel Electrode Material for Supercapacitor. *Appl. Phys. A Mater. Sci. Process.* **2021**, *127*, 2–11. [CrossRef]
31. Chen, C.; Deng, H.; Wang, C.; Luo, W.; Huang, D.; Jin, T. Petal-like CoMoO4Clusters Grown on Carbon Cloth as a Binder-Free Electrode for Supercapacitor Application. *ACS Omega* **2021**, *6*, 19616–19622. [CrossRef] [PubMed]
32. Wang, X.; Zhang, J.; Ma, D.; Feng, X.; Wang, L.; Wang, B. Metal-Organic Framework-Derived Trimetallic Nanocomposites as Efficient Bifunctional Oxygen Catalysts for Zinc-Air Batteries. *ACS Appl. Mater. Interfaces* **2021**, *13*, 33209–33217. [CrossRef] [PubMed]
33. Zhu, Y.; Guo, H.; Wu, Y.; Cao, C.; Tao, S.; Wu, Z. Surface-Enabled Superior Lithium Storage of High-Quality Ultrathin NiO Nanosheets. *J. Mater. Chem. A* **2014**, *2*, 7904–7911. [CrossRef]
34. Zheng, J.H.; Zhang, R.M.; Yu, P.F.; Wang, X.G. Binary Transition Metal Oxides (BTMO) (Co-Zn, Co-Cu) Synthesis and High Supercapacitor Performance. *J. Alloys Compd.* **2019**, *772*, 359–365. [CrossRef]
35. Akhavan, O. Photocatalytic Reduction of Graphene Oxides Hybridized by ZnO Nanoparticles in Ethanol. *Carbon N. Y.* **2011**, *49*, 11–18. [CrossRef]
36. Chen, Y.; Xu, X.L.; Zhang, G.H.; Xue, H.; Ma, S.Y. A Comparative Study of the Microstructures and Optical Properties of Cu- and Ag-Doped ZnO Thin Films. *Phys. B Condens. Matter* **2009**, *404*, 3645–3649. [CrossRef]
37. Potlog, T.; Duca, D.; Dobromir, M. Temperature-Dependent Growth and XPS of Ag-Doped ZnTe Thin Films Deposited by Close Space Sublimation Method. *Appl. Surf. Sci.* **2015**, *352*, 33–37. [CrossRef]
38. Nagaraju, P.; Alsalme, A.; Alkathiri, A.M.; Jayavel, R. Rapid Synthesis of WO_3/Graphene Nanocomposite via in-Situ Microwave Method with Improved Electrochemical Properties. *J. Phys. Chem. Solids* **2018**, *120*, 250–260. [CrossRef]
39. Thangavel, S.; Elayaperumal, M.; Venugopal, G. Synthesis and Properties of Tungsten Oxide and Reduced Graphene Oxide Nanocomposites. *Mater. Express* **2012**, *2*, 327–334. [CrossRef]
40. Thakur, A.K.; Limaye, M.V.; Rakshit, S.; Maity, K.N.; Gupta, V.; Sharma, P.K.; Singh, S.B. Controlled Synthesis of WO_3 Nanostructures: Optical, Structural and Electrochemical Properties. *Mater. Res. Express* **2018**, *6*, 025006. [CrossRef]
41. Thiyagarajan, K.; Muralidharan, M.; Sivakumar, K. Defects Induced Magnetism in WO_3 and Reduced Graphene Oxide-WO_3 Nanocomposites. *J. Supercond. Nov. Magn.* **2018**, *31*, 117–125. [CrossRef]
42. Vinoth, S.; Wang, S.F. Modification of Glassy Carbon Electrode with Manganese Cobalt Oxide-Cubic like Structures Incorporated Graphitic Carbon Nitride Sheets for the Voltammetric Determination of 2,4,6 -Trichlorophenol. *Microchim. Acta* **2022**, *189*. [CrossRef] [PubMed]
43. Jagadale, A.D.; Kumbhar, V.S.; Lokhande, C.D. Supercapacitive Activities of Potentiodynamically Deposited Nanoflakes of Cobalt Oxide (Co_3O_4) Thin Film Electrode. *J. Colloid Interface Sci.* **2013**, *406*, 225–230. [CrossRef] [PubMed]
44. Kondalkar, V.V.; Yang, S.S.; Patil, P.S.; Choudhury, S.; Bhosale, P.N.; Lee, K.K. Langmuir-Blodgett Assembly of Nanometric WO_3 Thin Film for Electrochromic Performance: A New Way. *Mater. Lett.* **2017**, *194*, 102–106. [CrossRef]
45. Wang, S.; Xu, Y.; Qin, J.; Chen, S.; Du, Y.; Xu, Y.; Xu, J.; Zhou, W. One-Pot Synthesis of MnX2O4(X = Co, Ni)/Graphite Nanoflakes Composites as High-Performance Supercapacitor Electrodes. *Mater. Res. Bull.* **2021**, *141*. [CrossRef]
46. Xu, K.; Ma, S.; Shen, Y.; Ren, Q.; Yang, J.; Chen, X.; Hu, J. CuCo2O4 Nanowire Arrays Wrapped in Metal Oxide Nanosheets as Hierarchical Multicomponent Electrodes for Supercapacitors. *Chem. Eng. J.* **2019**, *369*, 363–369. [CrossRef]
47. Sheng, R.; Hu, J.; Lu, X.; Jia, W.; Xie, J.; Cao, Y. Solid-State Synthesis and Superior Electrochemical Performance of MnMoO4 Nanorods for Asymmetric Supercapacitor. *Ceram. Int.* **2021**, *47*, 16316–16323. [CrossRef]
48. Lin, J.H.; Chen, H.; Shuai, M.M.; Wu, W.Z.; Wang, Y.; Zhang, W.G.; Ling, Q.D. Facile Synthesis of the 3D Interconnecting Petal-like $NiCoO_2$/C Composite as High-Performance Supercapacitor Electrode Materials. *Mater. Today Nano* **2019**, *7*, 3–10. [CrossRef]
49. Wang, D.; Jiang, S.; Duan, C.; Mao, J.; Dong, Y.; Dong, K.; Wang, Z.; Luo, S.; Liu, Y.; Qi, X. Spinel-Structured High Entropy Oxide $(FeCoNiCrMn)_3O_4$ as Anode towards Superior Lithium Storage Performance. *J. Alloys Compd.* **2020**, *844*, 156158. [CrossRef]

50. Singh, A.K.; Sarkar, D.; Karmakar, K.; Mandal, K.; Khan, G.G. High-Performance Supercapacitor Electrode Based on Cobalt Oxide-Manganese Dioxide-Nickel Oxide Ternary 1D Hybrid Nanotubes. *ACS Appl. Mater. Interfaces* **2016**, *8*, 20786–20792. [CrossRef]
51. Patil, P.D.; Shingte, S.R.; Karade, V.C.; Kim, J.H.; Dongale, T.D.; Mujawar, S.H.; Patil, A.M.; Patil, P.B. Effect of Annealing Temperature on Morphologies of Metal Organic Framework Derived NiFe2O4 for Supercapacitor Application. *J. Energy Storage* **2021**, *40*, 102821. [CrossRef]
52. Zhang, Y.Z.; Zhao, J.; Xia, J.; Wang, L.; Lai, W.Y.; Pang, H.; Huang, W. Room Temperature Synthesis of Cobalt-Manganese-Nickel Oxalates Micropolyhedrons for High-Performance Flexible Electrochemical Energy Storage Device. *Sci. Rep.* **2014**, *5*, 8536. [CrossRef] [PubMed]
53. Biswal, A.; Panda, P.K.; Acharya, A.N.; Mohapatra, S.; Swain, N.; Tripathy, B.C.; Jiang, Z.T.; Minakshi Sundaram, M. Role of Additives in Electrochemical Deposition of Ternary Metal Oxide Microspheres for Supercapacitor Applications. *ACS Omega* **2020**, *5*, 3405–3417. [CrossRef] [PubMed]
54. Huo, W.C.; Liu, X.L.; Yuan, Y.S.; Li, N.; Lan, T.; Liu, X.Y.; Zhang, Y.X. Facile Synthesis of Manganese Cobalt Oxide/Nickel Cobalt Oxide Composites for High-Performance Supercapacitors. *Front. Chem.* **2019**, *7*, 661. [CrossRef]
55. Liu, Y.; Ma, Z.; Xin, N.; Ying, Y.; Shi, W. High-Performance Supercapacitor Based on Highly Active P-Doped One-Dimension/Two-Dimension Hierarchical NiCo2O4/NiMoO4 for Efficient Energy Storage. *J. Colloid Interface Sci.* **2021**, *601*, 793–802. [CrossRef]
56. Zhao, Y.; Hu, L.; Zhao, S.; Wu, L. Preparation of MnCo2O4@Ni(OH)2 Core–Shell Flowers for Asymmetric Supercapacitor Materials with Ultrahigh Specific Capacitance. *Adv. Funct. Mater.* **2016**, *26*, 4085–4093. [CrossRef]
57. Yang, F.; Guo, H.; Chen, Y.; Xu, M.; Yang, W.; Wang, M.; Yang, M.; Zhang, J.; Sun, L.; Zhang, T.; et al. Ultrahigh Rate Capability and Lifespan MnCo2O4/Ni-MOF Electrode for High Performance Battery-Type Supercapacitor. *Chem. A Eur. J.* **2021**, *27*, 14478–14488. [CrossRef]
58. Dhas, S.D.; Maldar, P.S.; Patil, M.D.; Waikar, M.R.; Sonkawade, R.G.; Chakarvarti, S.K.; Shinde, S.K.; Kim, D.Y.; Moholkar, A.V. Probing the Electrochemical Properties of NiMn2O4 Nanoparticles as Prominent Electrode Materials for Supercapacitor Applications. *Mater. Sci. Eng. B Solid-State Mater. Adv. Technol.* **2021**, *271*, 115298. [CrossRef]
59. Huang, Y.Y.; Lin, L.Y. Synthesis of Ternary Metal Oxides for Battery-Supercapacitor Hybrid Devices: Influences of Metal Species on Redox Reaction and Electrical Conductivity. *ACS Appl. Energy Mater.* **2018**, *1*, 2979–2990. [CrossRef]
60. Chen, X.; Xin, N.; Li, Y.; Sun, C.; Li, L.; Ying, Y.; Shi, W.; Liu, Y. Novel 2D/2D NiCo2O4/ZnCo2O4@rGO/CNTs Self-Supporting Composite Electrode with High Hydroxyl Ion Adsorption Capacity for Asymmetric Supercapacitor. *J. Mater. Sci. Technol.* **2022**, *127*, 236–244. [CrossRef]
61. Manohar, A.; Vijayakanth, V.; Prabhakar Vattikuti, S.V.; Kim, K.H. Synthesis and Characterization of Mg^{2+} Substituted $MnFe_2O_4$ Nanoparticles for Supercapacitor Applications. *Ceram. Int.* **2022**, *48*, 30695–30703. [CrossRef]
62. Singh, G.; Kumar, Y.; Husain, S. Improved Electrochemical Performance of Symmetric Polyaniline/Activated Carbon Hybrid for High Supercapacitance: Comparison with Indirect Capacitance. *Polym. Adv. Technol.* **2021**, *32*, 4490–4501. [CrossRef]
63. Cai, Y.; Wang, Y.; Deng, S.; Chen, G.; Li, Q.; Han, B.; Han, R.; Wang, Y. Graphene Nanosheets-Tungsten Oxides Composite for Supercapacitor Electrode. *Ceram. Int.* **2014**, *40*, 4109–4116. [CrossRef]